Int. J. of Geosynth. and Ground Eng. (2016) 2:24
DOI 10.1007/s40891-016-0065-3

ORIGINAL ARTICLE

Improved Performance of Rail Track Substructure Using Synthetic Inclusions: Experimental and Numerical Investigations

Ngoc Trung Ngo[1] · **Buddhima Indraratna**[1]

Received: 7 July 2016 / Accepted: 30 July 2016 / Published online: 8 August 2016

Abstract Ballasted rail tracks offer the most important means of transporting bulk freight and passengers in terms of the sheer tonnage of traffic. Ballast is a prominent component of conventional rail infrastructure because it controls the stability and performance of track. Repetitive train loads degrade ballast grains due to breakage and the progressive accumulation of external fines or mud-pumping from the softer subgrade. They decrease the shear strength and drainage capacity of track embankments, while adversely affecting its safety and efficiency as speed restrictions are imposed and track maintenance becomes more frequent. Although synthetic inclusions such as geogrids and rubber mats placed between the ballast and subballast definitely improve track performance, further study is needed before incorporating them into existing design routines catering for future high speed trains and heavier haul trains. This paper presents the very latest knowledge of rail track geomechanics, including several important concepts and topics related to laboratory testing and discrete element modelling approaches to study the load and deformation of ballast improved by rubber mats and synthetic geogrids. This paper focuses on studies carried out at the University of Wollongong on track infrastructure, and includes examples whereby innovation progresses from theory to practice. Discrete element modelling is also used to carry out a micromechanical analysis of the ballast and geogrid interface to provide further insight into ballast subjected to shearing.

Keywords Ground improvement · Geosynthetics · Ballasted track · Discrete element method

✉ Buddhima Indraratna
indra@uow.edu.au

Ngoc Trung Ngo
trung@uow.edu.au

[1] Centre for Geomechanics and Railway Engineering, Faculty of Engineering and Information Sciences, ARC Centre of Excellence for Geotechnical Science and Engineering, University of Wollongong, Wollongong, NSW 2522, Australia

Introduction

Ballasted rail tracks are the major infrastructure for freight and passenger transport in Australia, with a 33,400 km long network that provides a vital supply chain for agriculture and the mining industries. Traditional railway foundations are now overloaded due to an increasing demand for heavier and faster trains that have accelerated the deterioration of track substructure and increased the maintenance costs [1]. Ballast is a free-draining granular material that serves as a load bearing layer in rail tracks whose major main functions are: (a) to transmit induced loads to the underneath layer at a reduced and acceptable level of stress, (b) provide lateral resistance, and (c) facilitate free drainage conditions. Ballast under heavy traffic loading undergoes irrecoverable plastic deformation and particle degradation [2], which results in sharp angular grains which degrade into relatively less angular or semi-rounded particles that ultimately reduce inter-particle friction, while decreasing the load carrying capacity of track [1, 3, 4]. The inability of current tracks in many parts of Australia to support increasingly heavier and faster trains is a major concern because the high cyclic and impact loads lead to ballast degradation, and the infiltration of fine particles such as coal dust and soft subgrade soils contaminate the overlying ballast and decrease its porosity, thus impeding track drainage [5]. Moreover, as trains pass over the tracks the ballast aggregates spread laterally due to

inadequate confining pressure from the shoulder ballast and also deteriorate as the angular corners and sharp edges break. As a result, ballast becomes fouled, less angular, and its shear strength decreases [3]. Budiono et al. [6] report that fine particles adversely influence the strength and stiffness of track structure because as the amount of fouling increases, the stiffness of ballast decreases. These issues result in excessive track settlement and instability, as well as high maintenance costs. Because of track degradation, the Australian rail industry has a very large budget in terms of frequent track repair and maintenance, as well as significant ground improvement efforts where soft and saturated subgrade poses challenges. A large proportion of track maintenance costs are related to problems with the substructure such as ballast breakage, fouling, poor drainage, differential settlement, and track buckling [7]. Hence, there is a definite need for innovative design solutions that can extend the service life of tracks and cater for faster and heavier traffic.

Use of Geosynthetics in Ballasted Tracks

The aforementioned problems can be mitigated by utilising planer geosynthetics (geogrids, geotextiles, geocomposite); three-dimensional cellular reinforcement (geocells) and energy absorbing rubber mats [2, 8]. The ability of geosynthetics to improve track stability has been the subject of numerous experimental investigations carried out by Bathurst and Raymond [9], McDowell et al. [10], Shukla and Yin [11], Brown et al. [12], Shukla [13], Biswas et al. [14], Kwon and Penman [15], among others. Geosynthetics lead to more resilient long term performance of rail track, as well as helping with drainage and reducing ballast degradation [4, 16, 17]. The ability of geogrids to provide additional confinement to granular materials has been emphasized by numerous studies [e.g., 5, 8, 9, 18, 19]; their studies show that the interaction between ballast and geogrid is one of the most influential factors affecting the overall performance of geogrid-reinforced ballasted tracks. Geogrid confines the surrounding grains of ballast via frictional resistance that is mobilised between the ballast aggregates and subgrade layers, which then increases the stiffness of the surrounding particles. The shearing resistance of ballast increases as the particles interlock through the geogrid apertures. However, as ballast fouls, the influence of geogrids may decrease substantially as fine particles clog its openings and act like an impermeable lubricant which reduces the interlocking and frictional resistance between the geogrid and ballast [20].

Use of Rubber Mats in Ballasted Tracks

Geogrids placed under ballast do not absorb impact loads or perform well when placed under stiff foundations such as concrete bridge decks or level crossings; in fact ballast used in these places experiences significant degradation, despite the use of geogrids [21]. Rubber mats have recently been trialed in Europe for track substructure under stiff foundations to minimise the deformation and degradation of ballast aggregates and enhance overall track stability [22, 23]. The ability of rubber mats (shock mats) to absorb energy could reduce the amount of energy transferred to the ballast and other substructure components and thus ensure the track substructure experiences less deformation and degradation [21, 24]. The ability of shock mats to reduce noise along stiff tracks such as concrete bridges and tunnels, and control vibration along open tracks has been studied by Auersch [25], and Anastasopoulos et al. [26]. While rubber mats are used in Europe to reduce rail noise and vibration in urban areas, there is no scientific basis for their use as inclusions to absorb energy from track movement. Preliminary studies conducted by UOW researchers [21] indicate that their performance depends on the type of substructure layering (e.g., soft soil, stiff clay, rock, etc.), their individual properties, the loading magnitude and frequency (i.e., axle loads and train speeds), and their energy-absorbing properties. These preliminary studies did show that rubber mats perform well under transition zones (e.g., stiff foundations) but they cannot be used under soft estuarine (coastal) terrains because they prevent proper track drainage.

This paper presents the results of laboratory testing where a large-scale direct shear box, track process simulation apparatus (TPSA), and impact testing apparatus are used to study the improved performance of fresh and fouled ballast using geogrids and rubber mats; it will be possible to modify the existing guidelines to compensate for this adverse fouling effect. Moreover, numerical modelling using the discrete element method (DEM) is also presented to provide an insight into the contact force distributions and the evolution of contact anisotropy which cannot be measured in the laboratory.

Laboratory Studies for Geosynthetic Reinforced Ballast

Large-Scale Direct Shear Test

The large-scale direct shear test in this current study consists of a 300 × 300 mm^2 square steel box, 200 mm high, divided horizontally into two equal halves, as shown in Fig. 1a. In this test normal stresses are applied onto a floating load plate on top of the shear box via a system of dead weights attached to a lever arm. A displacement dial gauge is attached to the centre of the top plate to measure the deformation of ballast, another displacement dial gauge

(a)

(b)

Fig. 1 Large-scale laboratory apparatus: **a** direct shear box and **b** track process simulation apparatus (TPSA)

is attached to the lower half of the box to measure horizontal displacement during shearing, and a calibrated load cell is attached horizontally to measure the shear force. Tests are carried out at four normal loads of 1.33, 2.41, 4.57, and 6.73 kN, which correspond to normal stresses of 15, 27, 51 and 75 kPa, respectively. The materials in this study are given in Fig. 2. Samples of ballast samples came from Bombo quarry, New South Wales, Australia, and then cleaned and sieved according to the Australia Standard [27]. Polypropylene biaxial geogrid with 40 mm × 40 mm apertures is used in this study (tensile strength at 2 and 5 % strains are 10.5 and 21 kN/m, respectively). Coal fines used as fouling material in the tests are provided by the Queensland Rail. The levels of ballast fouling are quantified with the void contamination index (VCI) introduced earlier by Tennakoon et al. [7], which includes the void ratio, the specific gravity and gradation of ballast and fouling material. VCI is defined by:

$$\mathrm{VCI} = \frac{(1+e_\mathrm{f})}{e_\mathrm{b}} \times \frac{G_\mathrm{sb}}{G_\mathrm{sf}} \times \frac{M_\mathrm{f}}{M_\mathrm{b}} \times 100, \quad (1)$$

where e_b, G_sb and M_b are the void ratio, the specific gravity and the dry mass of clean ballast, respectively, and e_f, G_sf and M_f are the void ratio, specific gravity and dry mass of the fouling material.

The particle size distribution curves of ballast and coal fines used in this experiments are presented in Fig. 3. The ballast aggregates placed into the bottom half of the shear box, were compacted into two layers by a vibratory compactor to a unit weight of 15.5 kN/m^3. After the first layer has been compacted, a sheet of geogrid is placed on top and the overhanging material is secured to the lower sides by clamping blocks and nails to simulate a non-displacement boundary. To mimic a fouling condition in the field, a predetermined amount of coal fines is spread uniformly on top of each layer of compacted ballast, and then an air hose is used to gently blow the fines into the ballast voids. Upon vibration induced compaction, these coal fines then migrated and accumulated under gravity into voids between the particles of ballast. The remaining ballast is then added to the upper half of the shear box and compacted to achieve the desired unit weight. The lower section of the shear box is moved horizontally at 2.5 mm/min while the upper section of the box remains stationary. Each specimen is then subjected to a horizontal displacement of $\Delta h = 37$ mm (e.g., 12.3 % shear strain, which is the maximum movement allowed by the test apparatus). The shear stresses and vertical strains at corresponding shear strains are measured during the shearing process.

Figure 4 shows the shear stress versus horizontal displacement responses of fresh and fouled ballast with and without geogrid, under varying normal stresses. The results show that the peak shear stress of the specimens reinforced by geogrid is more than the unreinforced specimens due to the grains of ballast interlocking with the geogrid. The peak shear stress generally increases as the normal stress increases, and decreases as the level of fouling increases (i.e., VCI). Moreover there is a significant decrease in the peak shear stresses because fines fill voids and coat the surfaces of the particles; this inhibits inter-particle friction and decreases the shearing resistance at the geogrid–ballast interface. Ballast reinforced by geogrid generally shows less dilation than fresh ballast because the mechanical interlock at the ballast–geogrid interface minimizes the movement of particles [2]. All the tests show a relatively

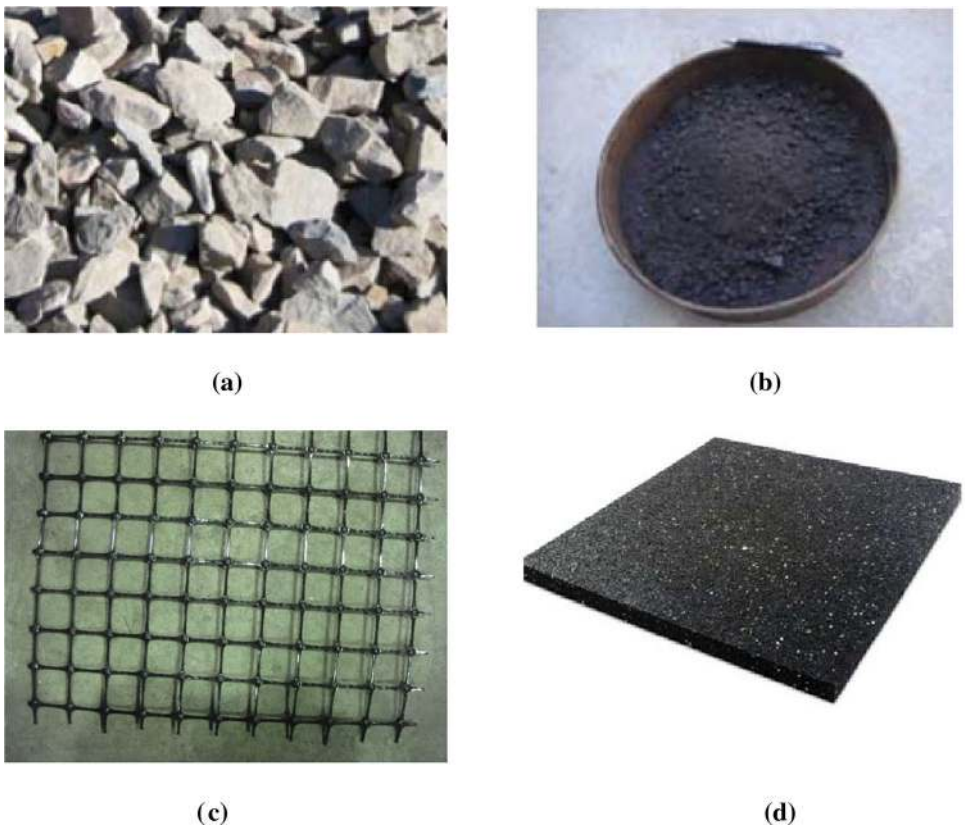

Fig. 2 Materials tested in laboratory: **a** fresh ballast, **b** coal fines, **c** biaxial geogrid, 40 × 40 mm, and **d** rubber mat

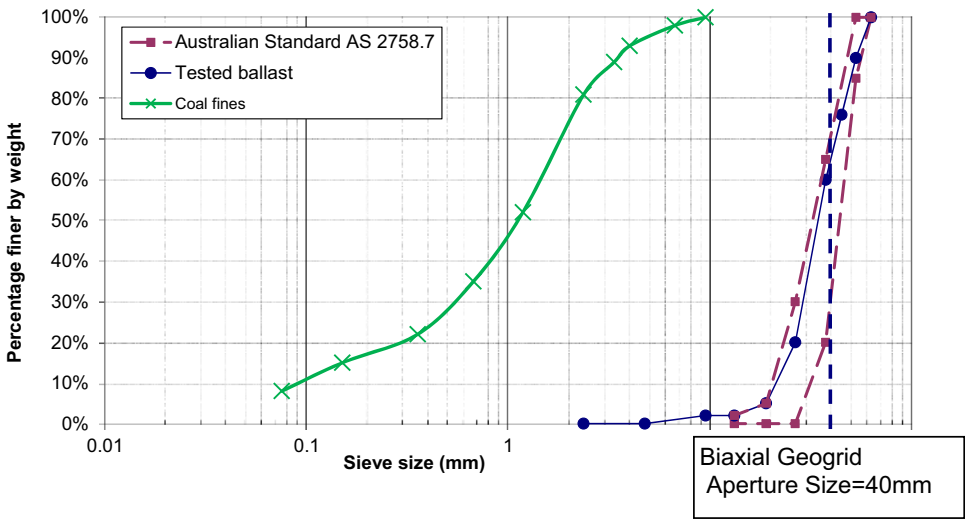

Fig. 3 Gradations of materials tested in laboratory

low initial compression followed by dilation. When the ballast aggregates compress to a threshold packing arrangement, subsequent shearing would initiate dilation associated with strain softening. Hence tests indicate that while the geogrid establishes an effective interlock which reduces dilation, it has almost no effect on compression because the geogrid used here is thin and flexible.

Track Process Simulation Apparatus (TPSA)

A large-scale TPSA, 800 mm long × 600 mm wide × 600 mm high was built at the University of Wollongong to simulate the response of ballasted tracks to cyclic loading, as shown in Fig. 1b. Further details of this apparatus can be found in Indraratna et al. [5]. A 50 mm thick layer of

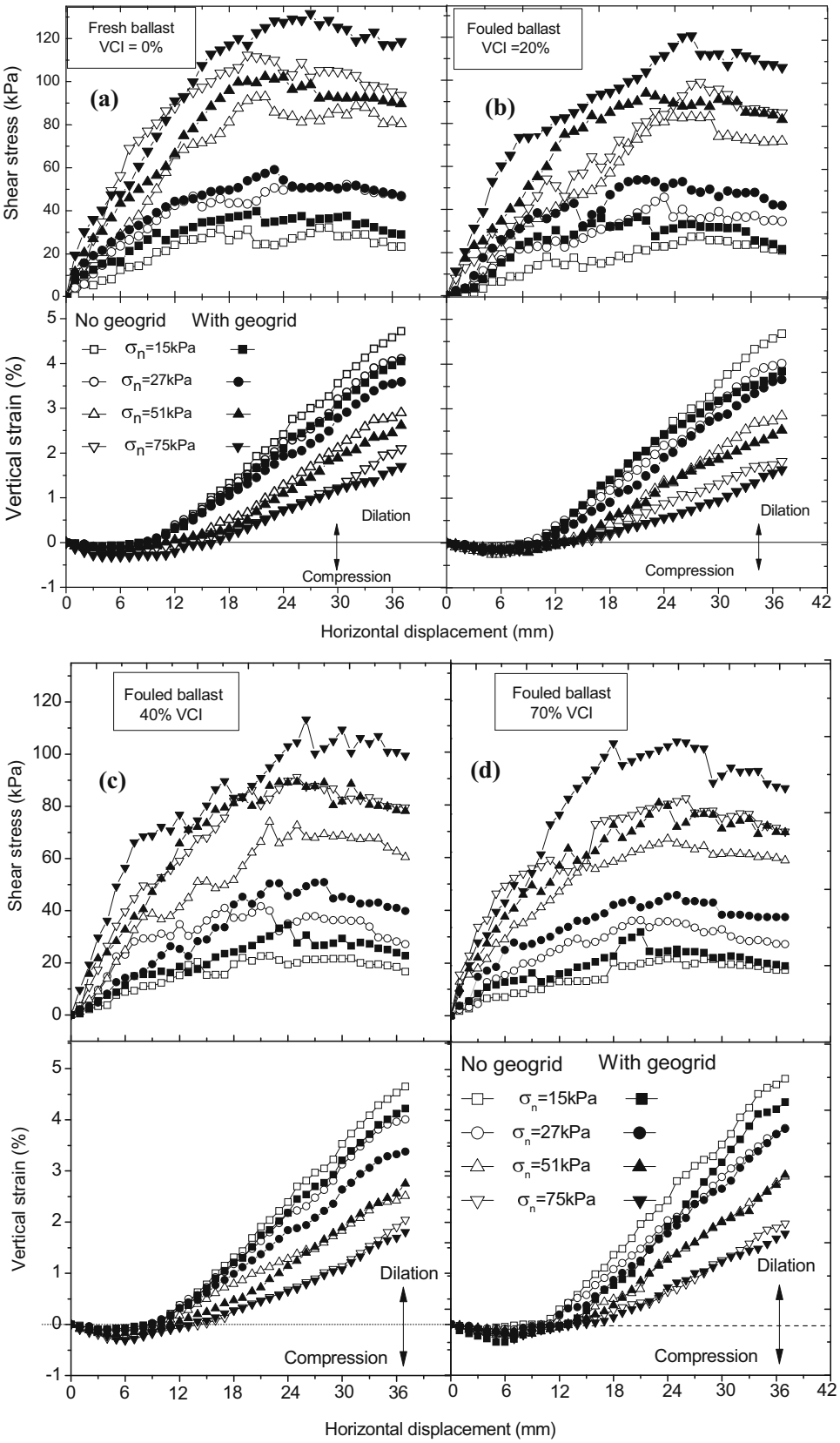

Fig. 4 Shear stress–displacement behaviour of fresh and fouled ballast: **a** fresh ballast, **b** VCI = 20 %, **c** VCI = 40 %, and **d** VCI = 70 % (modified after Indraratna et al. [3])

compacted clay layer is placed at the bottom of the apparatus, followed by a 100 mm thick capping layer, a 300 mm thick layer of load bearing ballast, and then a 150 mm layer of crib ballast. Finally, a 650 mm long × 220 mm wide concrete sleeper and a segment of rail are placed above this compacted ballast. The capping layer is a compacted mixture of fine gravel and sand ($d_{50} = 0.26$ mm, $C_u = 5$). All the samples of fresh and coal fouled ballast are prepared by following the gradation curves given in Fig. 3 (e.g., $d_{50} = 35$ mm, $C_u = 1.6$). A layer of geogrid reinforcement (aperture size 40 mm × 40 mm) is then placed at the ballast–capping interface. After preparing the specimen, relatively small confining pressures ($\sigma'_2 = 10$ kPa and $\sigma'_3 = 7$ kPa) are applied to the walls of the TPSA by hydraulic jacks to simulate shoulder ballast and field confining stresses. A cyclic load is then applied with a maximum load intensity of 73 kN to produce the same average contact stress at the sleeper–ballast interface as a typical 25 tonne/axle traffic load. The tests are carried out at 15 Hz to simulate a train speed of 80 km/h. The number of load cycles applied in each test is 500,000, but due to the brevity of this paper, only some of the test results are summarised and discussed here. More detailed procedures and the complete findings and discussions from these tests are reported elsewhere by Indraratna et al. [5].

Figure 5 shows the accumulated settlement of fresh and fouled ballast assemblies with and without geogrid at varying load cycles. Ballast reinforced with geogrid generally shows reduced settlement compared to the unreinforced assembly for any given VCI, and as expected, an increasing level of fouling results in increasing ballast deformation. All the samples experience an initial rapid settlement up to 100,000 cycles, followed by gradually increasing settlement within 300,000 cycles, and they then remain relatively stable to the end (500,000 cycles). This indicates that ballast undergoes a lot of rearrangement and densification during the initial load cycles, but when the grains attain a threshold compression, any subsequent loading would resist settlement and promote dilation unless particle crushing occurs [3]. The measured data is best interpreted by Fig. 5c which shows the final values of settlement at $N = 500{,}000$ for ballast reinforced with geogrid and unreinforced ballast, with a varying VCI. In this instance the benefit due to geogrid decreases as the VCI increases, and then becomes marginal when the VCI >40 %.

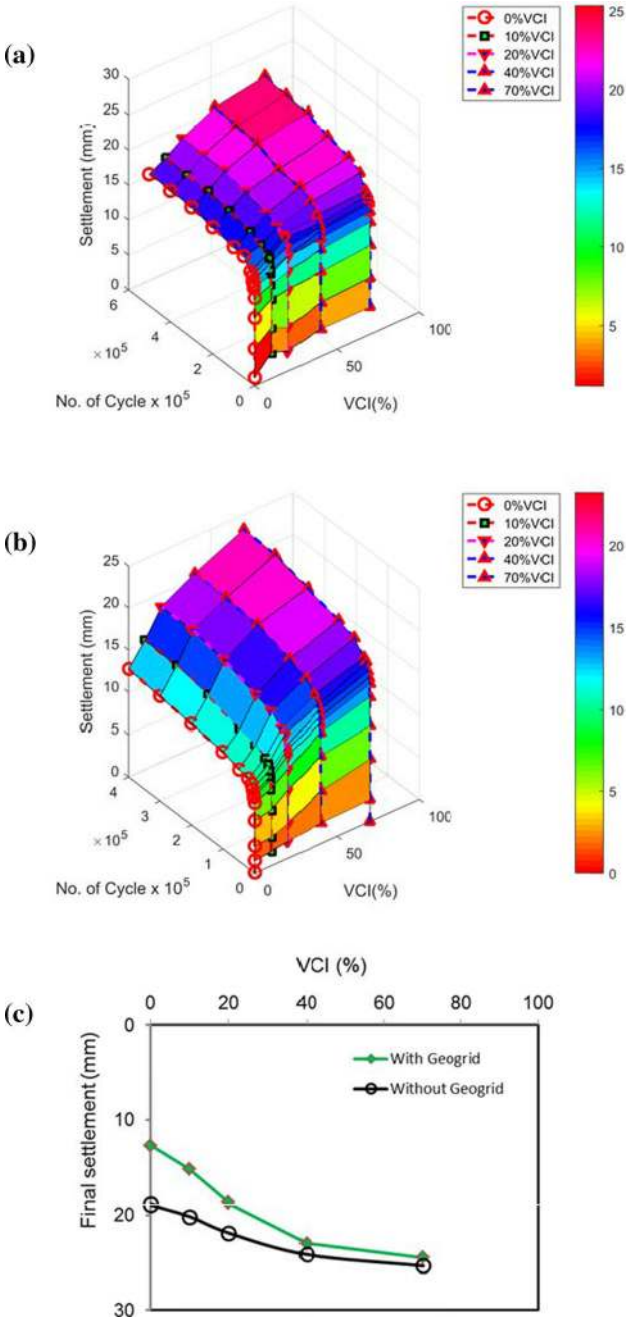

Fig. 5 Measured settlements of fresh and fouled ballast with and without geogrid: **a** no geogrid, **b** with geogrid, and **c** final settlements versus VCI

Drop-Weight Impact Testing Apparatus

Track substructures are often subjected to impact loads due to abnormalities in the wheel or rail such as wheel-flat, dipped rails, turnouts, crossings, insulated joints, imperfect rail welds and rail corrugations, among other factors. These impact loads are of a high magnitude and very short duration, depending on the nature of the wheel or rail irregularities, and on the dynamic response of the track [2, 28]. The large scale drop-weight impact testing equipment at UOW consists of a 5.81 kN free fall hammer that can be dropped from a maximum height of 6 m with an equivalent maximum drop velocity of 10 m/s (Fig. 6); it is used in this study to study how impact loads affect the deformation of ballast. The hammer is lifted mechanically to the required

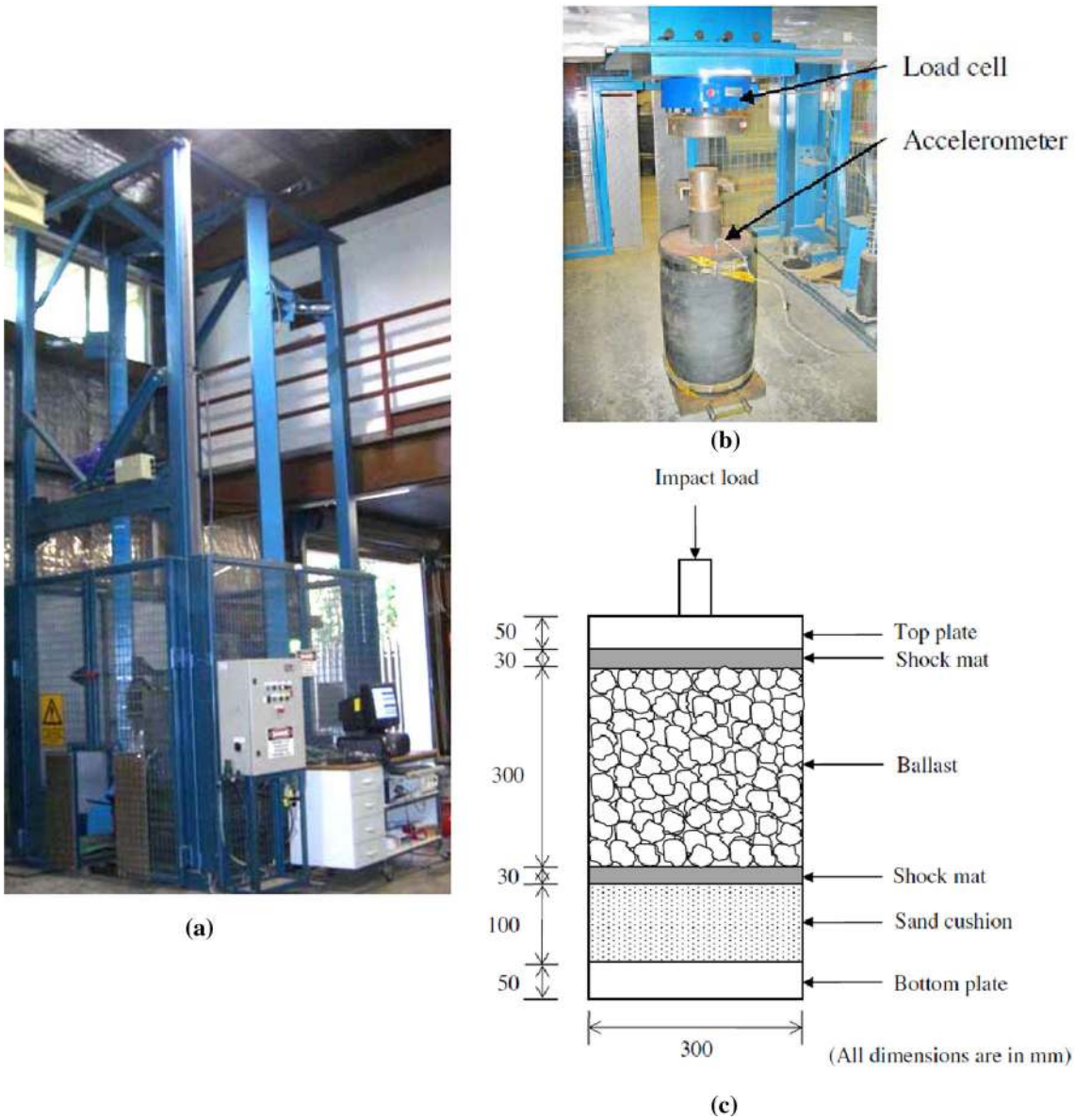

Fig. 6 Impact testing system apparatus: **a** perspective view of the equipment, **b** ballast specimen, and **c** schematic diagram of a typical test specimen

drop height and released by an electronic quick release system. To eliminate any surrounding noise and ground motion, the isolated concrete foundation (5.0 m × 3.0 m × 2.5 m) has a much higher fundamental frequency than the test apparatus. Ballast specimens 300 mm in diameter by 300 mm high are used in the laboratory (Fig. 6b, c). The material specifications and test procedures are given elsewhere by Nimbalkar et al. [29]. To simulate a low confining pressure in the field, the test specimens are confined in a rubber membrane thick enough to prevent it being pierced by sharp particles during testing. A rigid circular steel plate (thickness $t = 50$ mm) is used to represent a stiff subgrade (i.e., a bridge deck), where a thin layer of compacted sand is used to simulate relatively weak subgrade conditions. The 10 mm thick rubber mat used in the study was made from 1 to 3 mm size recycled rubber granulates bound by a polyurethane elastomer compound (tensile strength = 600 kN/m^2, tensile strain at failure = 80 %, compressive strain = 3800 kN/m^2). During testing, the transient impact forces are recorded by a dynamic load cell (capacity of 1200 kN) placed on the drop-weight hammer. A piezoelectric accelerometer is used to record the transient accelerations, and sample deformations are measured after each blow by electronic potentiometers.

Two distinct force peaks appear during impact loading, i.e., an instantaneous sharp peak with very high frequency

known as P_1, and a gradual peak of smaller magnitude and with a relatively lesser frequency, known as P_2. The impact force P_1 stems from the inertia of the rail and sleepers that resist the downward motion of the wheel, and this leads to compression in the contact zone between the wheel and the rail. The force P_2 prevails over a longer duration and is attributed to the mechanical resistance of the track substructure leading to its significant compression. Force P_2 directly influences the degradation of ballast grains and is determined by Australian standards as given by:

$$P_2 = P_0 + 2\alpha V_m \sqrt{\frac{M_u}{M_u + M_t}} \cdot \left[1 - \frac{C_t \pi}{4\sqrt{K_t(M_u + M_t)}}\right] \cdot \sqrt{K_t M_u}, \quad (2)$$

where P_0 is the maximum static wheel load, M_u is the vehicle unsprung mass per wheel (kg), 2α is the total dip angle (rad), V_m is the maximum normal operating velocity (m/s), M_t is the equivalent vertical rail mass per wheel (kg), K_t is the equivalent vertical rail stiffness per wheel (N/m) and C_t is the equivalent vertical rail damping per wheel (N s/m).

The impact load–time response subjected to the first drop of the free-fall hammer is presented in Fig. 7 where two distinct types of force peaks P_1 and P_2 can be observed. Here, multiple P_1 type peaks followed by the distinct P_2 type peak often occur, and then there is a remarkable increase of P_2 at the initial stages of impact loading but then it becomes almost insignificant. This shows that the ballast mass stabilises after being impacted a certain number of times to produce an almost constant P_2. The benefits of a rubber mat are therefore twofold: (i) it attenuates the impact force, and (ii) it decreases the impulse frequencies and thus extends the duration of each impact. The vertical and lateral deformation of the ballast are recorded after each blow where the shear strain (ε_s) and volumetric strain (ε_v) of ballast with and without the inclusion of rubber mats are shown in Fig. 8, where the shear strain and volumetric strain increase with successive impacts. The inclusion of rubber shock mats placed at the top and bottom of the ballast reduce the shear and volumetric strains quite significantly (i.e., in the order of 40–50 %), but with weak subgrade this improvement is less marked. Placing shock mats at the top and bottom of the ballast mass significantly reduces the strains induced by impact.

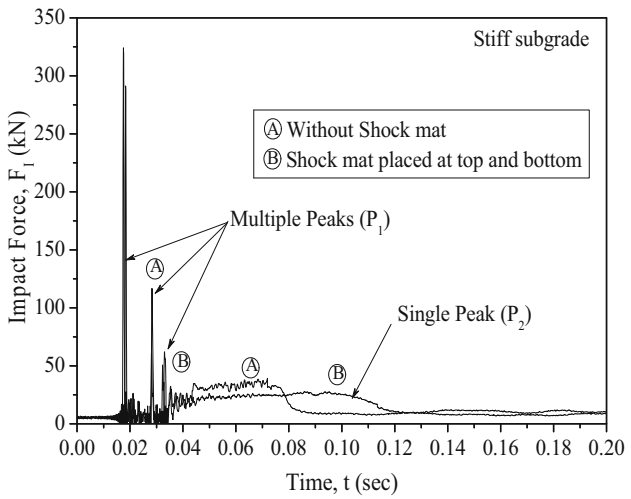

Fig. 7 Typical impact force responses measured in laboratory (modified after Nimbalkar et al. [29])

Discrete Element Modelling

The DEM has been used to investigate the shear stress and strain of ballast fouled with clay; DEM is often used to model ballast because it captures the discrete nature of

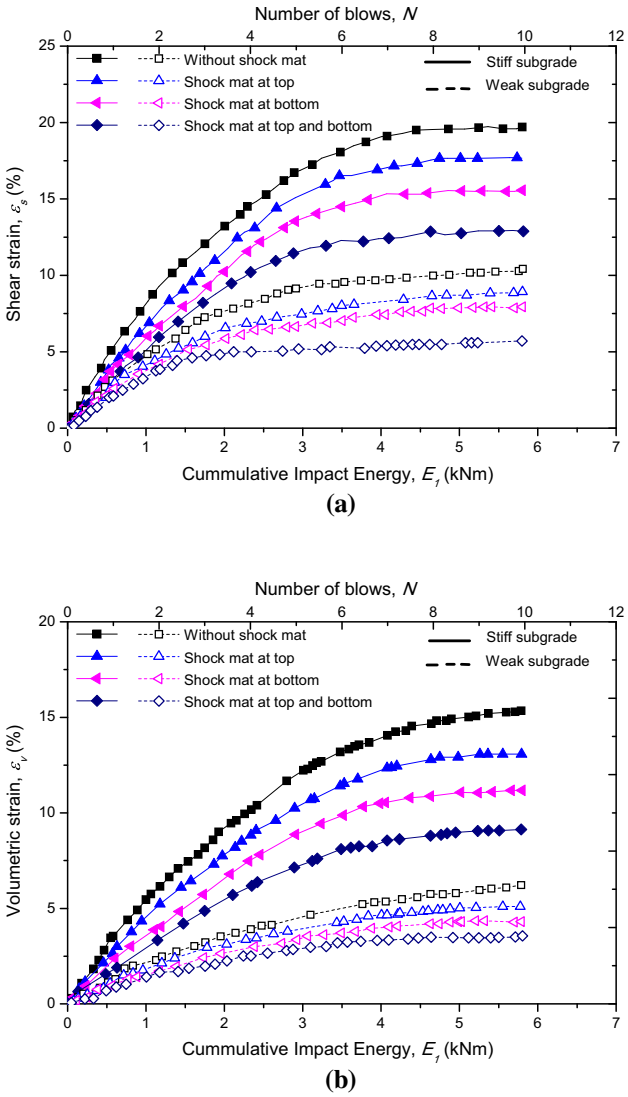

Fig. 8 Measured shear and volumetric strain behaviour of ballast with and without shock mat for stiff and weak subgrade: **a** shear strain, and **b** volumetric strain (modified after Nimbalkar et al. [29])

particulate materials [30, 31], and it can examine the mechanical behaviour of a granular assembly that consists of a collection of arbitrarily shaped discrete particles subjected to quasi-static and dynamic conditions [17, 32]. In DEM, the force–displacement law derives the contact force acting on two particles in contact to the relative displacement between them [33], so if particle B with a radius $R^{[B]}$ is in contact with particle A with radii $R^{[A]}$ (Fig. 9), or in contact with a wall, the particle penetration depth (U^n) is defined as:

$$U^n = \begin{cases} R^{[A]} + R^{[B]} - d, & \text{(particle}-\text{particle)}, \\ R^{[B]} - d, & \text{(particle}-\text{wall)}, \end{cases} \tag{3}$$

where d is the distance between the particle and particle centres, given as:

$$d = \left| x_i^{[B]} - x_i^{[A]} \right| = \sqrt{\left(x_i^{[B]} - x_i^{[A]} \right)\left(x_i^{[B]} - x_i^{[A]} \right)}. \tag{4}$$

The location of the contact point is given by:

$$x_i^{[C]} = \begin{cases} x_i^{[A]} + \left(R^{[A]} - \frac{1}{2}U^n \right) n_i, & \text{(particle}-\text{particle)}, \\ x_i^{[B]} + \left(R^{[B]} - \frac{1}{2}U^n \right) n_i, & \text{(particle}-\text{wall)}, \end{cases} \tag{5}$$

where n_i is the unit vector determined by:

$$n_i = \frac{x_i^{[B]} - x_i^{[A]}}{d}. \tag{6}$$

At a given time the force vector $\vec{F}$ that represents the interaction between the two particles is resolved into a normal ($\vec{F}_N$) and shear component ($\vec{F}_T$) with respect to the contact plane:

$$\vec{F}_N = K_N U^n, \tag{7}$$

$$\delta\vec{F}_T = -K_T \cdot \delta U^s, \tag{8}$$

where K_N and K_T is the normal and shear stiffness at the contact, δU^s is the incremental shear displacement, and $\delta\vec{F}_T$ is the incremental shear force. The new shear contact force is determined by summing the old shear force existing at the start of the time-step with the shear elastic force increment

$$\vec{F}_T \leftarrow \vec{F}_T + \delta\vec{F}_T \le \mu\vec{F}_N, \tag{9}$$

where μ is the coefficient of friction.

Modelling Laboratory Tests for Ballast in DEM

Figure 10 shows how DEM is used to model geogrid-reinforced ballast in a direct shear test and TPSA in a plane strain condition. The dimensions of the model are to the same as those carried out in the laboratory. Ballast grains with different shapes and sizes are modelled by lumping many spheres together to represent actual ballast gradation (Fig. 10a). This method is used by Lim and McDowell [34], Ngo et al. [35] to simulate ballast aggregates, which are then placed at random locations within the specified wall boundary and without overlapping. The micromechanical parameters used to model ballast, geogrid and coal fines are adopted from Indraratna et al. [16], as given in Table 1.

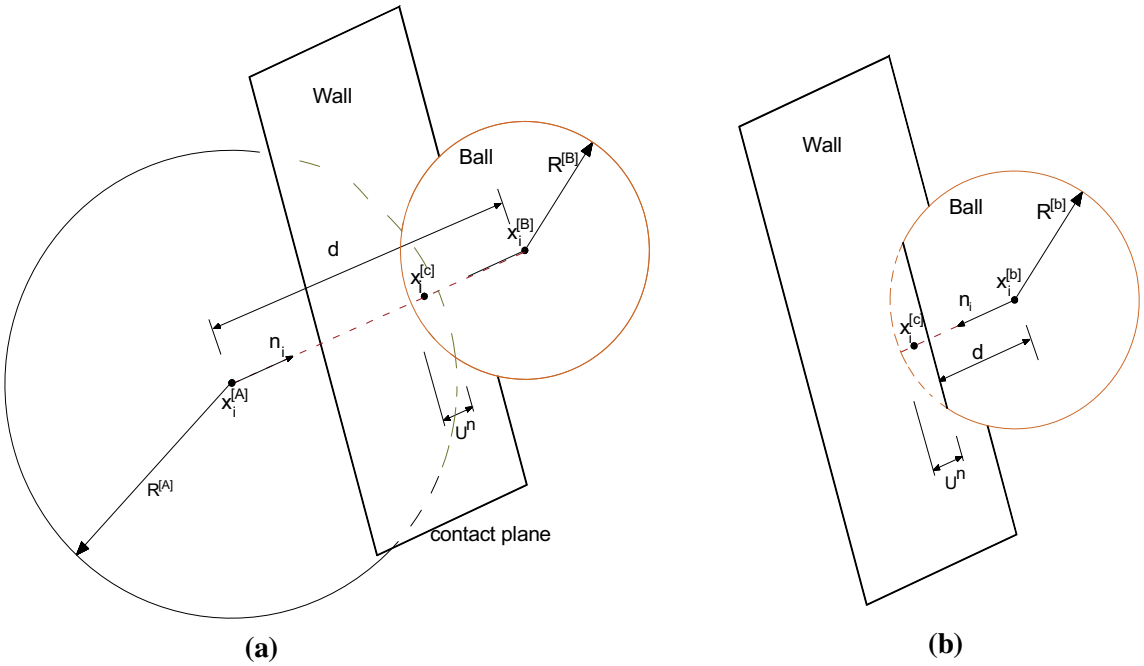

Fig. 9 Notation used to describe contacts in DEM: **a** ball–ball contact, and **b** ball–wall contact

DEM simulations of direct shear tests are carried out at three normal stresses of 27, 51, and 75 kPa for fresh and fouled ballast (VCI = 40 %) reinforced by geogrids. Figure 11 shows comparisons of shear stress–displacement responses of geogrid-reinforced ballast from the DEM analysis and those measured in the laboratory. Note that the results obtained from DEM agree reasonably well with the experimental results at a given normal stress and level of fouling. The strain softening behaviour of ballast and volumetric dilation can be seen in all simulations and indicate that the greater the normal stress (σ_n), the higher the peak stress and the smaller the dilation. The manner in which geogrid increases the shear strength of fresh and fouled ballast can be seen by comparing it with an assembly of unreinforced ballast.

DEM simulations of the TPSA in a plan strain condition are shown in Fig. 10d. The realistic shape and size of ballast grains and the procedures for simulating them in DEM are adopted from Indraratna et al. [36]; in this simulation clusters of bonded circular particles are used to model irregularly shaped grains of ballast, so the degradation of bonds within a cluster are considered to represent ballast breakage. Boundary conditions to simulate cyclic loads applied onto sleepers, lateral confining pressure applied onto vertical walls, and vertical pressure induced by the weight of crib ballast filling the gap between the vertical walls and sleeper

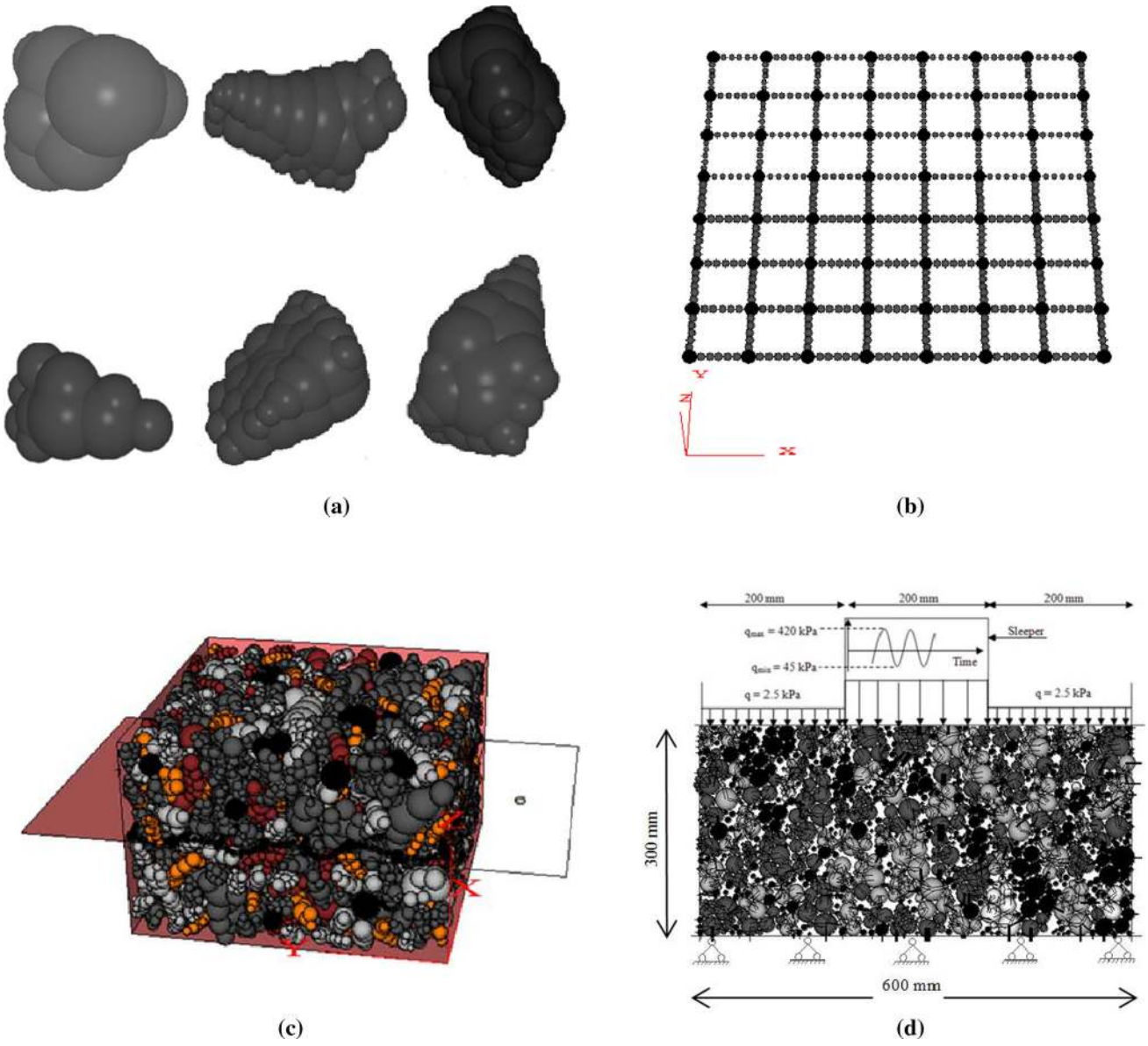

Fig. 10 Discrete element modelling of geogrid-reinforced ballast: **a** simulated ballast particles, **b** simulated biaxial geogrid, **c** large-scale direct shear box, and **d** track process simulation apparatus

Table 1 Micromechanical parameters of geogrid, ballast and coal fines adopted for DEM simulation

Parameters	Geogrid	Ballast	Coal fines
Particle density (kg/m^3)	800	2700	800
Coefficient of friction	0.5	0.8	0.2
Contact normal stiffness, K_N (N/m)	1.77×10^7	0.52×10^8	1.27×10^4
Contact shear stiffness, k_s (N/m)	0.88×10^7	0.52×10^8	1.27×10^4
Contact normal stiffness of wall-particle, $K_{N\text{-wall}}$ (N/m)	1×10^8	1×10^8	1×10^8
Shear stiffness of wall of wall-particle, $k_{s\text{-wall}}$ (N/m)	1×10^8	1×10^8	1×10^8
Parallel bond radius multiplier, r_p	0.5		
Parallel bond normal stiffness, k_{np} (kPa/m)	5.68×10^8		
Parallel bond shear stiffness, k_{sp} (kPa/m)	5.68×10^8		
Parallel bond normal strength, σ_{np} (MPa)	456		
Parallel bond shear strength, σ_{sp} (MPa)	456		

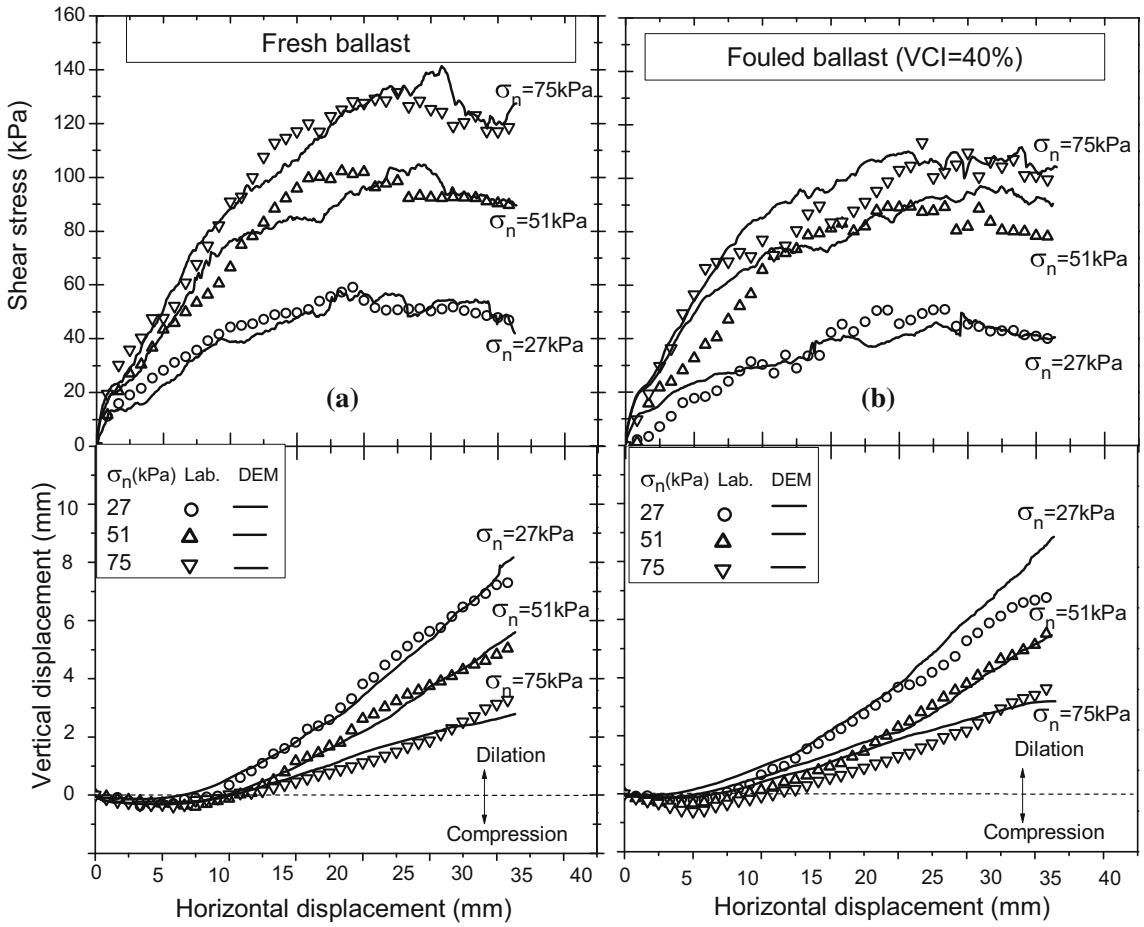

Fig. 11 Comparisons of shear stress–strain behavior of geogrid-reinforced ballast between experimental data and DEM simulation: **a** fresh ballast, and **b** fouled ballast (modified after Ngo et al. [17])

are shown in Fig. 10d. Cyclic tests for fresh and fouled ballast at VCI = 10, 20, 40 and 70 % are then simulated to a number of load cycles where $N = 4000$. During loading, the displacement of the top plate and the surrounding walls are recorded to determine the axial and associated volumetric strains. Figure 12 shows a comparison between the predicted and measured lateral displacement, settlement, and the number of broken bonds with the load cycles. This DEM simulation captures the load–deformation response of fouled ballast reasonably well. An increase in VCI leads to an increase in the lateral displacement of ballast and a subsequent increase in settlement. The DEM analysis also

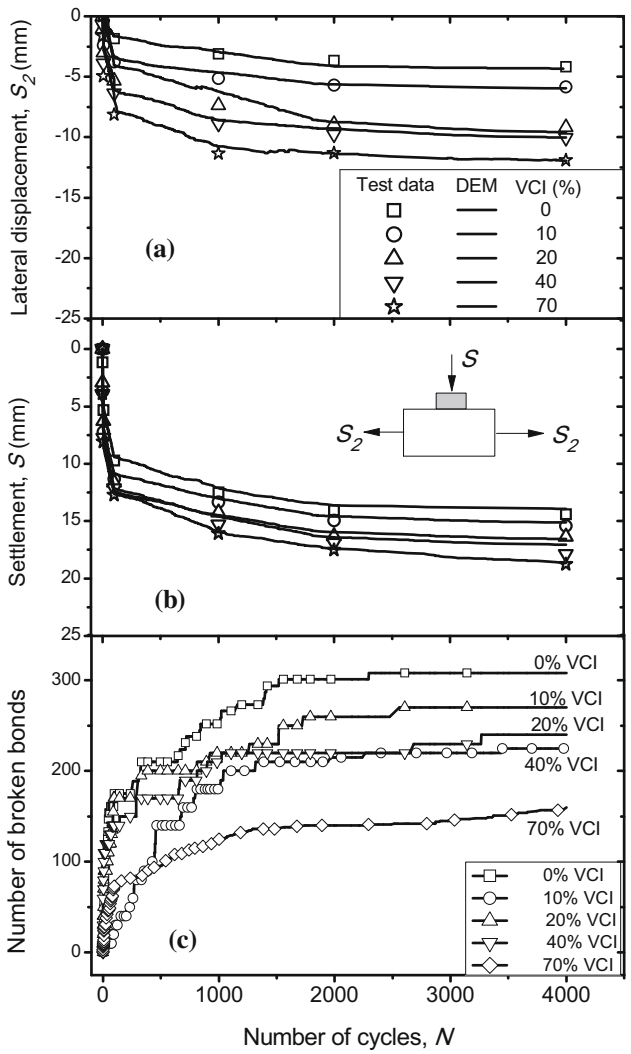

Fig. 12 Comparisons of lateral and vertical deformation between laboratory data and DEM simulations: **a** lateral displacement, **b** settlement, and **c** number of broken bonds

indicates that the accumulating number of broken bonds decreases as the VCI increases; this observation is justified of the fine particles in the voids could help to transfer the applied load more uniformly through the ballast skeleton and fine particles; in fact the contact forces transferred from ballast grains and through the fine particles in the fouled ballast matrix mimic the 'cushioning effect' of coal fines that effectively reduce the inter-particle contact stresses, and which in turn reduce particle breakage.

Micromechanical Analysis

The load transfer in a granular assembly depends on the orientation of contacts where an applied load is transmitted to ballast grains through an interconnected network of force chains at certain contact points [30]. When subjected to shearing, a ballast assembly induces changes in the contact forces and subsequently changes the number and orientation of the load-carrying contacts. A fabric tensor introduced by Rothenburg [37] is often used as an index to illustrate the packing structure of granular materials where the macroscopic stress–strain behaviour can be related to microscopic force and fabric parameters (i.e., stress–force–fabric relationship). To study the micromechanical behaviour of a granular assembly, Oda and Iwashita [30] introduced a second-order fabric tensor F_{ij} as given by:

$$F_{ij} = \int_{\Omega} E(\Omega) n_i n_j \mathrm{d}\Omega, \tag{10}$$

where n_i is the contact unit normal vector, $E(\Omega)$ is the contact distribution function, and $\mathrm{d}\Omega$ is an elementary solid angle in a spherical coordinate system.

By using angles γ, β in a spherical coordinate system, the fabric tensor F_{ij} can be written in an alternative form as:

$$F_{ij} = \int_0^{2\pi} \int_0^{\pi} n_i n_j E(\Omega) \sin\gamma \mathrm{d}\gamma \mathrm{d}\beta, \tag{11}$$

where, the ranges of γ and β are $0 \le \gamma \le \pi$ and $0 \le \beta \le 2\pi$, and $\sin\gamma \mathrm{d}\gamma \mathrm{d}\beta$ is a differential solid angle. The contact forces are often characterised by a density distribution of inter-particle contact orientation $E(\Omega)$, which can be approximated by a Fourier series approximation that can be further simplified as second-order tensors, as given below:

$$E(\Omega) = \frac{1}{4\pi}\left[1 + a_{ij}^{\mathrm{r}} n_i n_j\right]. \tag{12}$$

To study the directional distributions of contact forces, the density distribution of the average contact normal force ($\overline{f_i^{\mathrm{n}}}$) and shear force ($\overline{f_i^{\mathrm{s}}}$) in contact with the normal direction n_i can be captured using second order tensors, as given by:

$$\overline{f_i^{\mathrm{n}}}(n_i) = \overline{f^{\mathrm{n}}}(n_i) n_i = \overline{f_0}\left[1 + a_{\mathrm{kl}}^{\mathrm{n}} n_{\mathrm{k}} n_{\mathrm{l}}\right] n_i, \tag{13}$$

$$\overline{f_i^{\mathrm{s}}}(n_i) = \overline{f^{\mathrm{s}}}(n_i) t_i = \overline{f_0}\left[a_{ji}^{\mathrm{s}} n_j - \left(a_{\mathrm{kl}}^{\mathrm{s}} n_{\mathrm{k}} n_{\mathrm{l}}\right) n_i\right], \tag{14}$$

where a_{ij}^{r}, $a_{\mathrm{kl}}^{\mathrm{n}}$, and $a_{\mathrm{kl}}^{\mathrm{s}}$ are non-dimensional second-order tensors representing the coefficients of anisotropy, and f_0 is the average normal contact force.

Given that the TPSA is in a plane strain condition, contact force distributions can be described by the following Fourier series approximations proposed by Rothenburg [37], as given below:

$$E(\theta) = \frac{1}{2\pi}\left[1 + a^{\mathrm{r}} \cos 2(\theta - \theta_{\mathrm{r}})\right], \tag{15}$$

$$\overline{f^{\mathrm{n}}}(\theta) = \overline{f_0}\left[1 + a^{\mathrm{n}} \cos 2(\theta - \theta_{\mathrm{n}})\right], \tag{16}$$

$$\overline{f^{\mathrm{s}}}(\theta) = \overline{f_0}\left[-a^{\mathrm{s}} \cos 2(\theta - \theta_{\mathrm{s}})\right], \tag{17}$$

where a^{r}, a^{n}, and a^{s} are the coefficients of anisotropy of contact, the contact normal force and contact shear force,

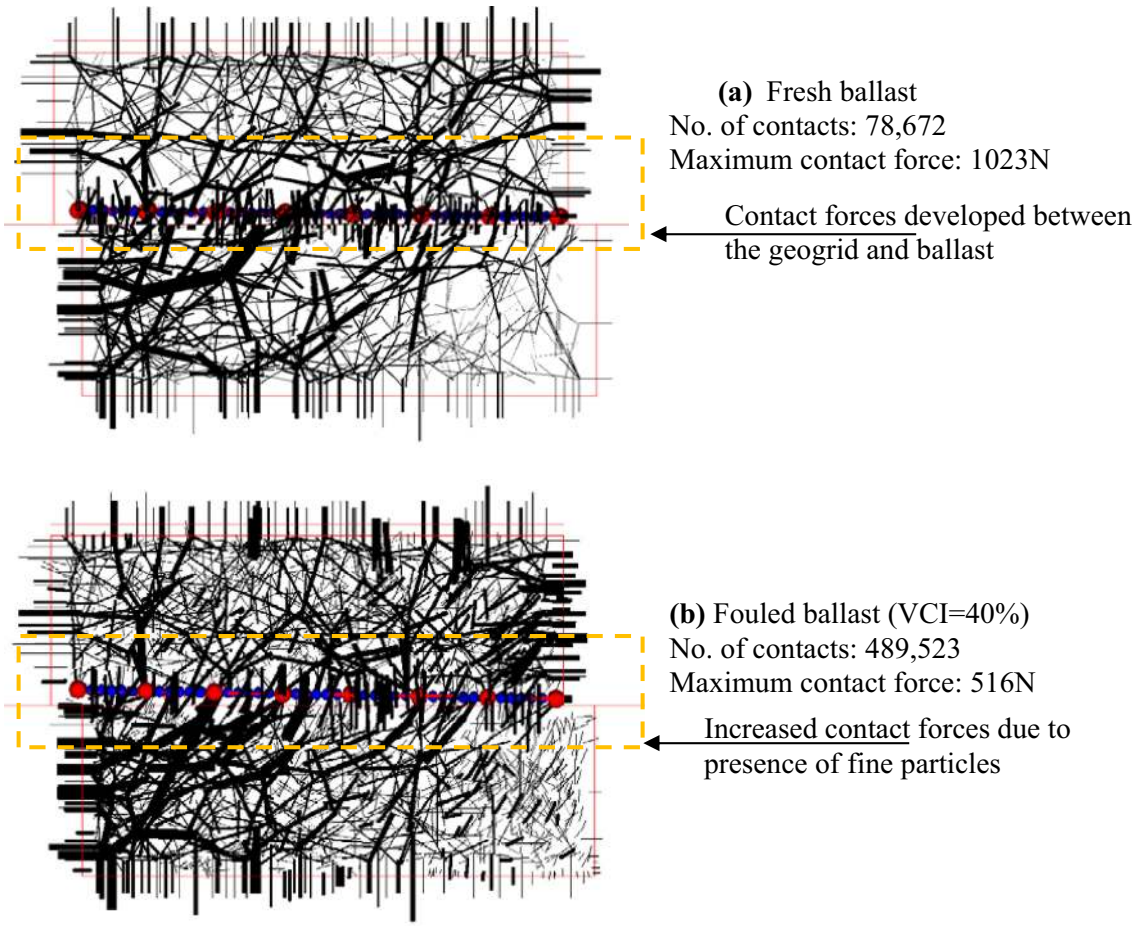

Fig. 13 Distribution of contact forces of fresh and 40 % VCI fouled ballast for a normal stress of 51 kPa at shear strain $\varepsilon_s = 6$ %, **a** fresh ballast, and **b** 40 % VCI fouled ballast

respectively, and θ_r, θ_n, and θ_s are the corresponding major principal directions of anisotropies, respectively.

The micromechanical analysis presented herein focusses on the evolution of contact force distributions of particles in the shear box and TPSA. As shearing took place during a direct shear test, the contact force distributions of fresh and fouled ballast (VCI = 40 %) at a shear displacement of 18 mm (i.e., shear strain of 6 %) are captured and presented in Fig. 13. Note that the fouled ballast exhibits denser contact chains and less maximum contact forces compared to those in the fresh ballast assembly (Fig. 13a). Note also that at the shearing plane, the contact forces developing between the geogrid and surrounding ballast grains are associated with significantly increasing number of contact forces [38], which could be attributed to the interlocking effect. Figure 14 shows the polar histogram of contact force distributions for fresh and fouled ballast (VCI = 40 %) simulated in the TPSA at different settlements S, from the DEM analysis, and those from the Fourier approximations. Polar histograms of the contact forces are obtained by collecting the contact force information at the predefined bin angle $\Delta\theta = 10°$. When the cyclic loads commence, the contact force anisotropy is coaxial with the vertical axes and has a principal direction of almost $\theta_n = 12°$ and 17° for fresh and fouled ballast, respectively, which is the major principal stress in the TPSA (Fig. 14a, d). An increase in settlement will allow the contact force chains to resist shear stresses and transfer the induced loads across the ballast assembly. Anisotropies of contact forces for ballast assemblies grow and rotate vigorously as shearing progresses, and reach their values of $\theta_n = 26°$, 31° at corresponding settlements of $S = 20$ mm (Fig. 14c, f). As settlement increases, the contact force anisotropies tend to align towards the horizontal axis as the number of contacts in a horizontal direction increase due to the particles spreading out laterally. This micromechanical information provides more insight into the orientation of contacts where the applied load is transmitted to a granular assembly through an interconnected network of forces that are difficult to measure in the laboratory.

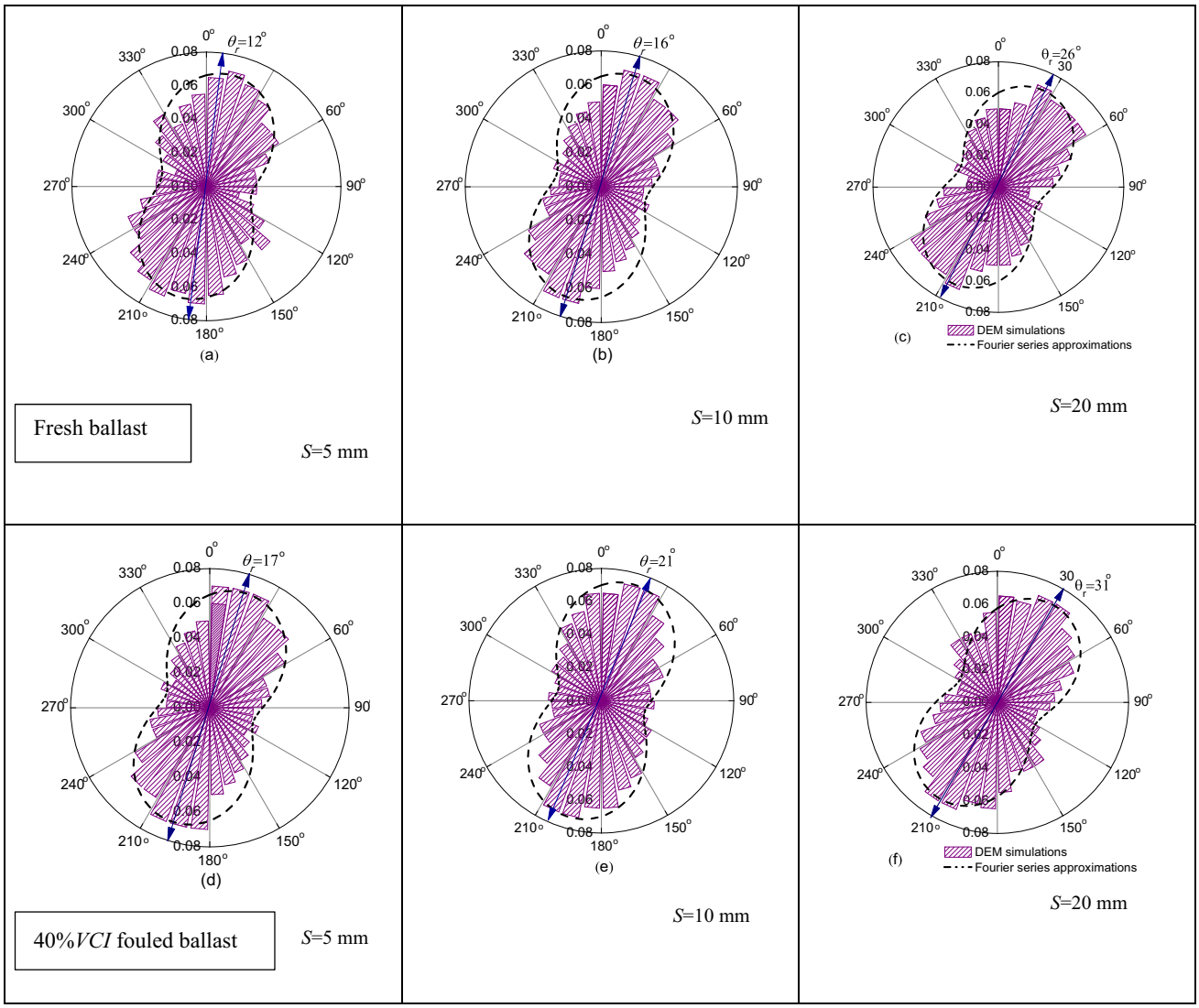

Fig. 14 Variations of contact force orientation of fresh and fouled ballast (VCI = 40 %) at varying settlements, $S = 5$, 10, 20 mm: **a–c** fresh ballast, and **d–f** fouled ballast

Conclusions

The performance of ballasted rail tracks with geogrids and shock mats has been investigated through large-scale laboratory testing and discrete element modelling. A series of large-scale laboratory tests using a direct shear box, TPSA and impact testing apparatus have been carried out. The role of geogrids and rubber mats in relation to stress–strain and the degradation of ballast have also been investigated. Data from laboratory tests indicate that geogrid increases the shear strength of ballast and reduces dilation due to interlocking between the ballast and geogrid which increases the peak shear stress and reduces the freedom of particles to displace. Coal fines in the ballast reduce the benefit gained from using geogrid as reinforcement because they fill the voids between the ballast particles and coat their surfaces, which reduce inter-particle friction and shearing resistance at the interface. The inclusion of rubber shock mats in ballasted track could improve the performance of ballast by attenuating the impact and thus mitigating degradation. A series of DEM simulations for large-scale direct shear tests and TPSA have been carried out for fresh and 40 % VCI coal-fouled ballast to study how its performance improved with geogrids. Without doubt the interlocking effect of ballast aggregates with the geogrid is the primary factor responsible for increasing the performance of a ballast assembly stabilised with geogrid. The results obtained from the DEM analysis agree with the measured data and show that the proposed DEM model could accurately capture the stress–displacement behaviour of ballast. A micromechanical analysis has also been carried out to investigate the orientation of the contact forces

and the fabric anisotropy of fresh and fouled ballast. The results from the simulations indicate that while the numbers of contacts increase significantly as the level of fouling increases the peak value of the contact force also decreases considerably. Under cyclic loads, contact force orientations will develop and rotate to resist the induced shear stresses and transmit loads across the ballast grains; this will change the direction of contact from being vertically orientated to being more horizontally orientated. This study provides a fundamental numerical framework that can easily be accommodated in design practices from a micromechanical perspective.

Acknowledgments The authors would like to thank the CRC for Rail Innovation for providing a PhD Scholarship and the financial support needed to undertake this research. The Authors also thank Associate Professor Cholachat Rujikiatkamjorn for useful discussions while preparing this paper. The Authors are grateful Mr. Alan Grant and Mr. Ian Bridge for their assistance in the laboratory and Dr. Nimbalkar for conducting impact tests. Some of the research outcomes reported in this paper are elaborated on in Journal of Geotechnical and Geoenvironmental Engineering: ASCE, International Journal of Geomechanics: ASCE, Computers and Geotechnics, Geotextiles and Geomembranes. The selected contents are reproduced with kind permission.

References

1. Selig ET, Waters JM (1994) Track geotechnology and substructure management. Thomas Telford, London
2. Indraratna B, Salim W, Rujikiatkamjorn C (2011) Advanced rail geotechnology—ballasted track. CRC Press, Taylor and Francis Group, London
3. Indraratna B, Ngo NT, Rujikiatkamjorn C (2011) Behavior of geogrid-reinforced ballast under various levels of fouling. Geotext Geomembr 29(3):313–322
4. Tutumluer E, Huang H, Bian X (2012) Geogrid-aggregate interlock mechanism investigated through aggregate imaging-based discrete element modeling approach. Int J Geomech 12(4):391–398
5. Indraratna B, Ngo NT, Rujikiatkamjorn C (2013) Studying the deformation of coal fouled ballast stabilised with geogrid under cyclic load. J Geotech Geoenviron Eng ASCE 139(8):1275–1289
6. Budiono DS, McSweeney T, Dhanasekar M, Gurung N (2004) The effect of coal dust fouling on the cyclic behaviour of railtrack ballast. In: Cyclic behaviour of soils and liquefaction phenomena. Taylor and Francis Group, London
7. Tennakoon N, Indraratna B, Rujikiatkamjorn C, Nimbalkar S, Neville T (2012) The role of ballast-fouling characteristics on the drainage capacity of rail substructure. Geotech Test J 35(4):1–11
8. Biabani MM, Indraratna B, Ngo NT (2016) Modelling of geocell-reinforced subballast subjected to cyclic loading. Geotext Geomembr 44(4):489–503
9. Bathurst RJ, Raymond GP (1987) Geogrid reinforcement of ballasted track. Transp Res Rec 1153:8–14
10. McDowell GR, Harireche O, Konietzky H, Brown SF, Thom NH (2006) Discrete element modelling of geogrid-reinforced aggregates. Proc ICE Geotech Eng 159(1):35–48
11. Shukla SK, Yin JH (2006) Fundamentals of geosynthetic engineering. Taylor and Francis Group, London
12. Brown SF, Kwan J, Thom NH (2007) Identifying the key parameters that influence geogrid reinforcement of railway ballast. Geotext Geomembr 25(6):326–335
13. Shukla SK (2012) Chapter 1: fundamentals of geosynthetics. In: Shukla SK (ed) Handbook of geosynthetic engineering, 2nd edn. ICE Publishing, London, pp 1–44
14. Biswas A, Ansari MA, Dash SK, Krishna AM (2015) Behavior of geogrid reinforced foundation systems supported on clay subgrades of different strengths. Int J Geosynth Ground Eng 1:20. doi:10.1007/s40891-015-0023-5
15. Kwon J, Penman J (2009) The use of biaxial geogrids for enhancing the performance of sub-ballast and ballast layers—previous experience and research. In: Bearing capacity of road, railways and airfields. Taylor and Francis Group, London
16. Indraratna B, Ngo NT, Rujikiatkamjorn C, Vinod J (2014) Behaviour of fresh and fouled railway ballast subjected to direct shear testing—a discrete element simulation. Int J Geomech ASCE 14(1):34–44
17. Ngo NT, Indraratna B, Rujikiatkamjorn C (2014) DEM simulation of the behaviour of geogrid stabilised ballast fouled with coal. Comput Geotech 55(2014):224–231
18. Alston C, Lowry DK, Lister A (2015) Geogrid reinforced granular pad foundation resting on loose and soft soils, Hamilton Harbour, Ontario. Int J Geosynth Ground Eng 1:21. doi:10.1007/s40891-015-0022-6
19. Palmeira EM, Góngora IG (2016) Assessing the influence of some soil–reinforcement interaction parameters on the performance of a low fill on compressible subgrade. Part I: fill performance and relevance of interaction parameters. Int J Geosynth Ground Eng 2:1. doi:10.1007/s40891-015-0041-3
20. Biabani MM, Ngo NT, Indraratna B (2016) Performance evaluation of railway subballast stabilised with geocell based on pull-out testing. Geotext Geomembr 44(4):579–591
21. Nimbalkar S, Indraratna B (2016) Improved performance of ballasted rail track using geosynthetics and rubber shockmat. J Geotech Geoenviron Eng 142(8):04016031
22. Ferreira PA, López-Pita A (2013) Numerical modeling of high-speed train/track system to assess track vibrations and settlement prediction. J Transp Eng 139(3):330–337
23. Costa PA, Calçada R, Cardoso AS (2012) Ballast mats for the reduction of railway traffic vibrations. Numerical study. Soil Dyn Earthq Eng 42:137–150
24. Lakuši S, Ahac M, Haladin I (2010) Experimental investigation of railway track with under sleeper pad. In: Proceedings of the 10th Slovenian road and transportation congress, pp 386–393
25. Auersch L (2006) Dynamic axle loads on tracks with and without ballast mats: numerical results of three-dimensional vehicle–track–soil models. Proc Inst Mech Eng F 220(2):169–183
26. Anastasopoulos I, Alfi S, Gazetas G, Bruni S, Leuven AV (2009) Numerical and experimental assessment of advanced concepts to reduce noise and vibration on urban railway turnouts. J Transp Eng ASCE 135(5):279–287
27. Australian Standard: AS 2758.7 (1996) Aggregates and rock for engineering purposes; Part 7: railway ballast. Sydney
28. Jenkins HM, Stephenson JE, Clayton GA, Morland JW, Lyon D (1974) The effect of track and vehicle parameters on wheel/rail vertical dynamic forces. Railw Eng J 3(1):2–16
29. Nimbalkar S, Indraratna B, Dash SK, Christie D (2012) Improved performance of railway ballast under impact loads using shock mats. J Geotech Geoenviron Eng 138(3):281–294
30. Oda M, Iwashita K (1999) Mechanics of granular materials: an introduction. A. A. Balkema, Rotterdam
31. O'Sullivan C (2011) Particulate discrete element modelling: a geomechanics perspective. Taylor and Francis, London

32. Lu M, McDowell GR (2008) Discrete element modelling of railway ballast under triaxial conditions. Geomech Geoeng Int J 3(4):257–270
33. Itasca Consulting Group, Inc. (2014) Particle flow code in three dimensions (PFC3D). Itasca Consulting Group, Inc., Minneapolis
34. Lim WL, McDowell GR (2005) Discrete element modelling of railway ballast. Granul Matter 7(1):19–29
35. Ngo NT, Indraratna B, Rujikiatkamjorn C, Biabani MM (2016) Experimental and discrete element modelling of geocell-stabilized subballast subjected to cyclic loading. J Geotech Geoenviron Eng 142(4):04015100-1–04015100-14
36. Indraratna B, Thakur PK, Vinod JS (2010) Experimental and numerical study of railway ballast behaviour under cyclic loading. Int J Geomech ASCE 10(4):136–144
37. Rothenburg L (1980) Micromechanics of idealized granular systems. PhD Dissertation, Carleton University, Ottawa
38. Ngo NT, Indraratna B, Rujikiatkamjorn C (2016) Modelling geogrid-reinforced railway ballast using the discrete element method. Transp Geotech. doi:10.1016/j.trgeo.2016.04.005